Published in final edited form as:
Neuroimage. Vol 56, Iss 3, Pages 1259-1266, 2011 DOI: 10.1016/j.neuroimage.2011.02.059

Track density imaging (TDI): validation of super-resolution property

Fernando Calamante [a,b,#], Jacques-Donald Tournier [a,b], Robin M. Heidemann [c], Alfred Anwander [c], Graeme D. Jackson [a,b], Alan Connelly [a,b]

[a] Brain Research Institute, Florey Neuroscience Institutes, Neurosciences Building, Banksia Street, Heidelberg West, Victoria 3081, Australia; and

[b] Department of Medicine, Austin Hospital, University of Melbourne, Melbourne, Australia.

[c] Max Planck Institute for Human Cognitive and Brain Sciences, Leipzig, Germany.

[#]Corresponding author:
Fernando Calamante
Brain Research Institute, Florey Neuroscience Institutes, Neurosciences Building, Austin Health, Banksia Street,
Heidelberg West, Victoria 3081, Australia,
Phone: (+61 3) 9496 2765, Fax: (+61 3) 9496 4071
http://www.brain.org.au.

ABSTRACT

We have recently introduced a novel MRI methodology, so-called super-resolution *track-density imaging* (TDI), which produces high-quality white matter images, with high spatial-resolution and exquisite anatomical contrast not available from other MRI modalities. This method achieves super-resolution by utilising the long-range information contained in the diffusion MRI fibre-tracks. In this study, we validate the super-resolution property of the TDI method by using *in vivo* diffusion MRI data acquired at ultra-high magnetic field strength (7 Tesla), and *in silico* diffusion MRI data from a well-characterised numerical phantom. Furthermore, an alternative version of the TDI technique is described, which mitigates the track-length weighting of the TDI map intensity. For the *in vivo* data, high-resolution diffusion images were down-sampled to simulate low-resolution data, for which the high resolution images serve as a gold-standard. For the *in silico* data, the gold-standard is given by the known simulated structures of the numerical phantom. Both the *in vivo* and *in silico* data show that the structures that could be identified in the TDI maps *only* after using super-resolution were consistent with the corresponding structures identified in the reference maps. This supports the claim that the structures identified by the super-resolution step are accurate, thus providing further evidence for the important potential role of the super-resolution TDI methodology in neuroscience.

Keywords: magnetic resonance imaging, super-resolution, white matter, fiber-tracking, diffusion MRI

ABBREVIATIONS

2D: two-dimensional;

3D: three-dimensional;

ADC: Apparent diffusion coefficient;

B_0: Main magnetic field;

CSD: constrained spherical deconvolution;

CST: corticospinal tract;

DEC: directionally-encoded colour.

FA: Fractional anisotropy;

FOD: fibre orientation distributions

FOV: field of view;

GRAPPA: GeneRalized Autocalibrating Partially Parallel Acquisition;

GS: gold standard;

iFOD2: 2nd order integration over fibre orientation distributions;

lmax: maximum harmonic order;

LR: low resolution;

*ls*TDI: length-scaled track-density imaging;

MCP: middle cerebellar peduncle;

SCP: superior cerebellar peduncle;

SLF: superior longitudinal fasciculus;

SNR, signal-to-noise ratio;

T1: longitudinal relaxation time;

T2: transverse relaxation time;

TDI: Track Density Imaging;

TE: echo-time;

TPF: transverse pontine fibres;

TR: repetition-time;

ZOOPPA: Zoomed imaging with GRAPPA.

INTRODUCTION

Over the years, considerable effort has been dedicated to developing new MR contrast mechanisms, improving image quality, and increasing the spatial resolution of images. The success of many of these efforts has led to an increasing role for MRI in neuroscience studies.

We have recently introduced a novel MRI methodology, so-called *super-resolution track-density imaging* (TDI), which produces high-quality white matter images, with very high spatial-resolution and anatomical contrast not available from other MRI modalities (Calamante et al., 2010). This method achieves super-resolution by utilising the long-range information contained in the diffusion MRI fibre-tracks, thus incorporating sub-voxel information: fibre-tracks (or streamlines) traverse a given voxel at specific spatial coordinates; the density of a large number of streamlines can then be used as intra-voxel information to generate an image with higher resolution than that of the acquired source diffusion MRI data. An important property of these TDI maps is their super-resolution nature: their spatial resolution and signal-to-noise ratio (SNR) can be adjusted depending on the chosen image resolution and the total number of fibre-tracks generated (see (Calamante et al., 2010) for further details).

Super-resolution methods have been used previously in MRI, including some controversial applications to diffusion MRI (Peled and Yeshurun, 2001; Scheffler, 2002; Peled and Yeshurun, 2002). All previous methods are based on the more commonly used super-resolution principle: the combination of information contained in multiple images acquired with relative sub-voxel shifts to reconstruct an image with higher resolution. Due to the band-limited nature of Fourier-encoded 2D-MRI data (Greenspan et al., 2002), it is generally accepted that this approach of combining sub-voxel shifted image can only achieve super-resolution in the slice direction. This limitation does not apply to the super-resolution TDI method since it relies on a different principle, namely that the additional information required can be obtained from modelling of fibre tracks.

As with any new technique offering super-resolution, the question arises as to the validity of the extra information generated. In particular, two questions naturally arise for the super-resolution TDI method: (1) Are the structures that appear following super-resolution processing an artefact of the super-resolution process itself? (2) Does the new MRI contrast observed in the TDI data identify real brain structures? The first question relates to *validation of the super-resolution property* of the TDI method, while the second relates to *validation of the anatomical information-content of the TDI contrast*.

In this study, we address the first question by using *in vivo* diffusion MRI data acquired at ultra-high magnetic field strength (7 Tesla). Ultra high-field MRI allows acquisition of higher spatial resolution images, due to the increased SNR associated with the higher magnetic field strength. At 7 Tesla, the higher SNR allows for the acquisition of diffusion MRI data at ~1 mm isotropic resolution, as compared to the more commonly used ~2.5 mm lower-resolution at 3 Tesla. This high-resolution data can be down-sampled to *simulate* diffusion MRI data that would have been acquired at lower resolution at 7 Tesla. Importantly, the original high-resolution diffusion MRI data can be used as a *reference* data-set for the down-sampled data-set. In this study, we generated TDI maps for both the high-resolution reference data-set and the down-sampled data-set, with super-resolution used *only* for the down-sampled data-set; note that the TDI map for the reference data-set can be considered the 'gold-standard', since super-resolution was not used in its creation. By comparing the resulting TDI maps, we aim to determine whether the same anatomical structures can be identified in both TDI maps, thus evaluating the super-resolution property.

As a further validation test, we also used *in silico* diffusion MRI data from a well-characterised numerical phantom (Close et al., 2009). This phantom was developed to generate numerical structures consisting of densely packed bundles of fibres representative of the complexity of human white matter, as well as to contain many realistic features such as tract kissing and crossing. For the *in silico* data, the gold-standard is given by the known structures of the phantom. Therefore, by comparing these structures with those observed in the super-resolution TDI map, the superresolution property can be once again evaluated.

MATERIALS AND METHODS

In vivo data acquisition

Diffusion MRI data were acquired from a healthy volunteer on a 7 Tesla whole-body MR scanner (MAGNETOM 7T, Siemens Healthcare, Erlangen, Germany) with a 24-element phased array head coil (Nova Medical, Wilmington, MA, USA). To achieve high resolution, a reduced field-of-view (FOV) acquisition ('zoomed') with GRAPPA parallel imaging acceleration was employed, a method known as Zoomed-imaging with GRAPPA (ZOOPPA) (Heidemann et al., 2010). Diffusion-weighted images were acquired with an optimized unipolar Stejskal-Tanner sequence (Stejskal and Tanner, 1965) with the following imaging parameters: TR = 9500 ms, TE = 72 ms, FOV = 141×191 mm², partial Fourier = 5/8, isotropic resolution 1 mm³, 71 slices with 10% overlap, b = 1000 s/mm², 60 diffusion-encoding directions. For outer-volume suppression a 'skewed' pulse was used as proposed in (Hwang et al, 1999; Pfeuffer et al., 2002) and for the GRAPPA reconstruction a 2D convolution kernel with three source-points along the readout direction and two source-points along phase-encoding direction was used with a GRAPPA acceleration factor of 3 (Note: the combination of Zoomed acquisition and GRAPPA resulted in a net acceleration factor of 4.26). A b=0 s/mm² volume was acquired first, and repeated after every 10 diffusion-weighted volumes. The whole protocol was repeated 6 times, for a total acquisition time of 69 min. For anatomical reference, a conventional 3D high-resolution T1-weighted image was also acquired (voxel size 0.8×0.8×0.8 mm_3). Informed written consent was obtained before the study in accordance with ethical approval from the ethics committee of the University of Leipzig.

In vivo diffusion MRI: data processing

The T1-weighted structural scan was used for skull-stripping, and the brain images were then co-registered into Talairach space (Talairach and Tournoux, 1988). The 42 images without diffusion-weighting distributed in the whole sequence were used to estimate motion correction parameters using rigid-body transformations (Jenkinson et al., 2002), implemented in FSL (FMRIB software library, University of Oxford, 2006. http://www.fmrib.ox.ac.uk/fsl). Motion correction for the 360 diffusion-weighted images was combined with a global registration to the T1 anatomy computed with the same method. The gradient direction for each volume was corrected using the rotation parameters. The registered images were interpolated to the new reference frame with an isotropic voxel resolution of 0.8 mm and the six corresponding acquisitions and gradient directions were averaged. For the remainder of this work, this 0.8 mm isotropic resolution diffusion MRI data-set will be our reference data-set and will be referred to as the 'gold-standard' (*GS*) dataset.

The combination of the shorter T2 and longer T1 at 7 Tesla, and the acquisition of higher-resolution images led to very low SNR levels in the diffusion MRI data. This introduced Rician bias in the magnitude data (Gudbjartsson and Patz, 1995) (NB. To avoid phase errors

when averaging multiple complex diffusion MRI data, magnitude averaging is commonly used). To minimise this effect, a Rician bias correction scheme was implemented similar to that described by Henkelman, based on an empirically determined lookup table (Henkelman, 1985).

The gold standard data set was down-sampled by a factor of 3 in each dimension to *simulate* a diffusion MRI data-set that would have been acquired at a lower resolution of 2.4 mm isotropic (see Fig. 1). For the remainder of this work, this 2.4 mm isotropic resolution diffusion MRI data-set will be referred to as the 'low resolution' (*LR*) dataset.

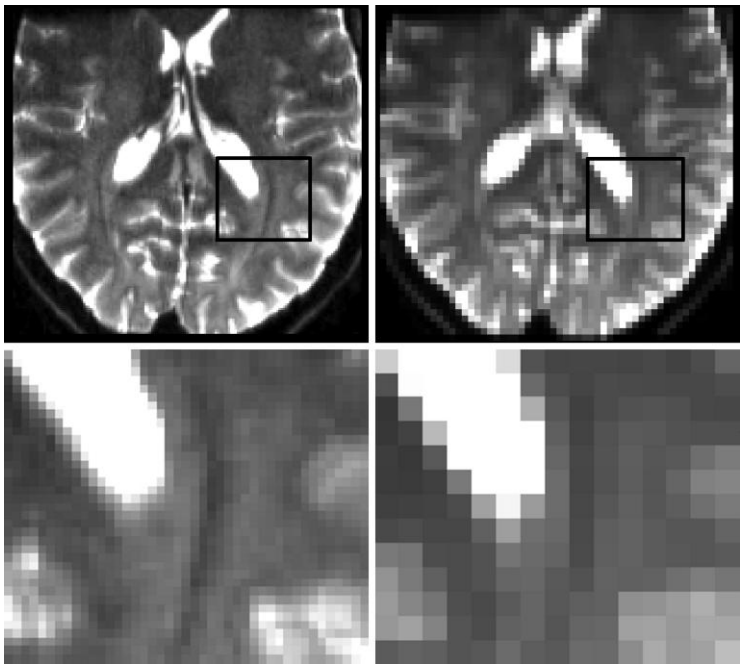

Fig. 1: Down-sample step for the *in vivo* data. Top-left: gold-standard (*GS*) diffusion MRI axial image (voxel size: 0.8 mm isotropic). Top-right: corresponding lower resolution (*LR*) down-sampled diffusion MRI image (voxel size: 2.4 mm isotropic). The bottom row shows zoomed versions of the regions indicated by the black rectangles in the corresponding top-row images. As can be appreciated, there is substantial loss of anatomical detail following the down-sampling step.

In silico data

The numerical phantom and the associated diffusion-weighted images were generated using the *Numerical Fibre Generator* (NFG) software package (Brain Research Institute, Melbourne, Australia, http://www.brain.org.au/software/) (Close et al., 2009). In particular, the structure used in this study corresponds to *Phantom A* in the pre-generated phantoms available from the NFG website, which corresponds to the phantom generated with the default parameters (Close et al., 2009). The corresponding simulated images were generated with a diffusion-weighted response function based on the diffusion tensor model with a fractional anisotropy FA = 0.8, apparent diffusion coefficient ADC = 9×10^{-4} mm²/s, and a *b*-value = 3000 s/mm² along 60 uniformly distributed diffusion-weighted directions, voxel size = 2 mm. Rician noise was added to generate SNR = 17.

Fibre-tracking

Whole-brain fibre-tracking (or whole-phantom fibre-tracking, for the *in silico* data) was performed using the *MRtrix* software package (Brain Research Institute, Melbourne, Australia, http://www.brain.org.au/software/). Constrained spherical deconvolution (CSD) (Tournier et al., 2007) was used to model multiple fibre orientations, and probabilistic tracking (Behrens et al., 2003) was performed using the 2^{nd} order integration over fibre orientation distributions (iFOD2) algorithm (Tournier et al., 2010). Whole-brain (or whole-phantom) tracking was performed by randomly seeding throughout the brain or throughout the numerical phantom (i.e. seed points were randomly defined in continuous space covering the whole brain or phantom) using the following relevant parameters: 1 mm step-size, maximum angle between steps = 45º, 3 FOD samples/step, any track with length < 10 mm (for the *in vivo* data) or < 4 mm (for the *in silico* data) was discarded, termination criteria: exit the brain (or the numerical phantom) or when the CSD fibre-orientation distribution amplitude was < 0.1. The primary parameter of interest in CSD is the maximum harmonic order l_{max} (which determines the 'sharpness' of the fibre orientation distributions) (Tournier et al., 2004; Tournier et al., 2007; Tournier et al., 2008); l_{max} = 10 (for the *in vivo* data) and 8 (for the *in silico* data) were employed in this study.

For the *in vivo* data, the complete analysis was performed for both the *GS* and the *LR* diffusion MRI data-sets. For the *in silico* data, the analysis was performed for the 2 mm data set. A total of 2,000,000 tracks were generated for each case.

Track-density Imaging (TDI)

In order to generate the TDI maps, the total number of tracks present in each element of a grid was calculated. It should be noted that the grid-element can be *smaller* than the source data voxel-size, and therefore the spatial resolution of the final map can be increased, i.e. super-resolution can be achieved by using the extra (long-range) information provided by the fibre-tracking results (Calamante et al., 2010).

For the *LR in vivo* data-set, a 0.8 mm isotropic grid was used to generate the super-resolution TDI (*super-TDI*$_{LR}$) map (i.e. the 2.4 mm source *LR* diffusion MRI data were super-resolved to construct a 0.8 mm TDI map). For comparison purpose, the corresponding TDI map without super-resolution (i.e. with a 2.4 mm isotropic grid) was also created (labelled as *TDI*$_{LR}$).

For the *GS in vivo* data-set, the same 0.8 mm isotropic grid was used to generate the corresponding TDI map; i.e. in this case, no super-resolution was introduced and the *TDI*$_{GS}$ map had the same resolution as the source *GS* diffusion MRI data. Therefore, the *super-TDI*$_{LR}$ and *TDI*$_{GS}$ maps have the same spatial resolution (0.8 mm), but *only* the *super-TDI*$_{LR}$ map was constructed using super-resolution. By comparing the brain structures in these maps, the effect of super-resolution can be evaluated, therefore addressing *question (1)* in the Introduction (i.e. the question related to the *validation of the super-resolution property* of the TDI method).

In summary, three TDI maps were calculated for the *in vivo* case:

- *TDI*$_{LR}$: 2.4 mm isotropic source diffusion data used to calculate a 2.4 mm isotropic TDI map
- *Super-TDI*$_{LR}$: 2.4 mm isotropic source diffusion data used to calculate a 0.8 mm TDI map

- TDI_{GS}: 0.8 mm isotropic source diffusion data used to calculate a 0.8 mm isotropic TDI map

To display also the local fibre directionality, the directionally-encoded colour (DEC) version of the TDI maps ((Calamante et al., 2010), which are the TDI equivalent of the DEC map in diffusion tensor imaging (Pajevic and Pierpaoli, 1999)) were also created for each case, with and without super-resolution. The colour-coding indicates the main local orientation, defined by averaging the colours of all the streamline segments contained within the grid element.

For the *in silico* data, a 0.2 mm isotropic grid was used to generate the super-resolution TDI (*super-* $TDI_{phantom}$) map (i.e. the 2 mm source diffusion MRI data were super-resolved to construct a 0.2 mm TDI map). Furthermore, for comparison purpose, the corresponding TDI map without super-resolution (i.e. with a 2 mm isotropic grid) was also created (labelled as $TDI_{phantom}$). For the phantom data, the gold-standard can be obtained from the known simulated structure. Given that the simulated phantom contains many white matter bundles with similar fibre density, the DEC TDI maps provide more contrast for the comparisons in the current study; these DEC TDI maps were created without super-resolution (2 mm grid) and with super-resolution (0.2 mm grid).

Modified TDI technique: length-scaled TDI

Shorter fibre-bundles will have fewer (randomly selected) seed points, and they will therefore generate fewer fibre tracks. In turn, the intensity of a grid element in the TDI map depends on the number of tracks traversing this grid element, and therefore shorter fibre bundles will have systematically reduced TDI intensity. Since a bi-directional tracking strategy was used in our study (i.e. tracking was done from each seed point in both directions), a simple way to normalise for this effect is to weight the contribution of each track to the intensity of the TDI map by the inverse of its length. We will refer to this version of the TDI map as *length-scaled TDI* (*ls*TDI). To investigate the effect of this strategy on the contrast of the TDI map, maps were also calculated using the above-mentioned normalisation, with the same grid resolutions as those used for the standard TDI method.

R E S U L T S

In vivo data

Fig. 2 shows an axial slice illustrating the typical image quality of each of the TDI maps. As can be appreciated in the figure, the super-resolution approach leads to a significant improvement in the image quality and anatomical detail (bottom row in the figure). For detailed assessment of the effects of super-resolution, see Figs. 3-5 below.

Fig. 3 shows an illustrative axial slice with a number of brain structures generated by the super-resolution step in the *super-*TDI_{LR} map in the parietal-occipital white matter; these structures are compared with the corresponding structures identified in the TDI maps calculated without super-resolution (TDI_{GS} and TDI_{LR}). As can be seen in this example, the structures generated by the super-resolution method are consistent with those observed in the gold-standard TDI map (TDI_{GS}). Note also that these structures are not apparent in the low resolution TDI_{LR} map, emphasising the power of the super-resolution method to retrieve anatomical information. The results from the corresponding DEC TDI maps support these findings, indicating that not only the structures, but also their directions are successfully reconstructed by the super-resolution step. To emphasise the level of improvement and degree of similarity between the gold-standard data and the super-resolution results, Figure 4

displays example profiles for the various TDI maps. For ease of comparison of these profiles, the TDI_{LR} map was linearly interpolated to the same resolution as the other two maps (i.e. 0.8 mm isotropic). As can be appreciated in this figure, the super-resolution results are able to replicate the various features ('mountains' and 'valleys') in the gold-standard profile; this is not the case for the interpolated low resolution data, for which many of the features are poorly characterized.

Two further illustrative examples at the level of the pons (Fig. 5) and at the level of the optic radiation (Fig. 6) are also shown, where the effect of super-resolution is compared with the results obtained without it.

In silico data

Fig. 7 shows an illustrative example of the DEC TDI maps (created both with and without super-resolution), as well as the corresponding simulated phantom (2 slices of the phantom are displayed). The figure shows the complexity of the structures in the phantom (top-row), and demonstrates how well super-resolution is able to recover many of the features of this complex structure (bottom-row); note also that these structures cannot be discerned in the TDI map created without super-resolution (middle-row). It should be noted that shorter fibre-bundles have reduced TDI intensity due to the lower number of seeds (and therefore tracks) generated in them (see Discussion), which explains the relatively low intensity of some of the peripheral short bundles in the numerical phantom (Fig. 6). This effect can be mitigated by using the *ls*TDI map, as shown in the next section.

Length-scaled TDI technique

Fig. 8 shows examples of the standard TDI maps and the corresponding *ls*TDI maps for the *in vivo* data. As can be seen in these images, the contrast on the two maps is different, with shorter tracks relatively lighter in the *ls*TDI map, and longer tracks relatively darker, when compared to the TDI map. Similar results were obtained for the *in silico* data, where the shorter bundles, which were dark in the original TDI map, now have a similar intensity to the rest of the tracks in the *ls*TDI map, leading to a more uniform overall signal intensity (Fig. 8, bottom row).

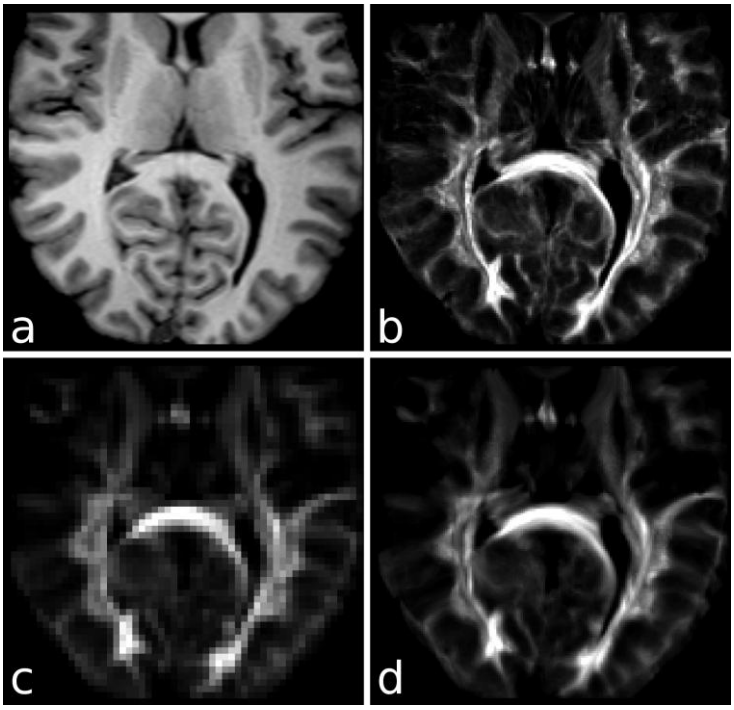

Fig. 2: TDI maps for the *in vivo* data. (a) Conventional T1-weighted image for anatomical reference. (b) Gold-standard TDI map (TDI_{GS}) with 0.8 mm isotropic resolution (calculated from 0.8 mm source diffusion MRI data). (c) Low-resolution TDI map (TDI_{LR}) with 2.4 mm isotropic resolution (calculated from 2.4 mm source diffusion MRI data). (d) Super-resolution TDI map ($superTDI_{LR}$) with 0.8 mm isotropic resolution (and calculated from 2.4 mm source diffusion MRI data). As shown in the figure, a significant improvement in image quality is achieved with super-resolution (see bottom row).

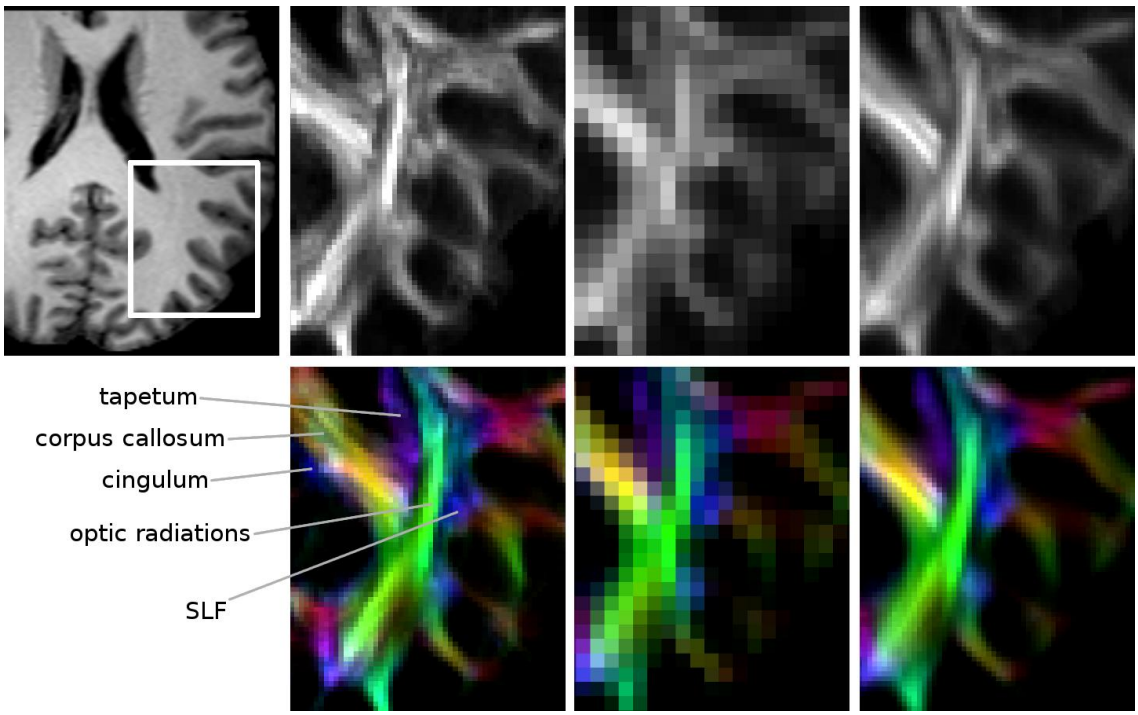

Fig. 3: Structures identified by the super-resolution step in the parietal-occipital white matter. Top row: (first column) anatomical T1-weighted image indicating the zoomed region shown in the TDI maps; (second column) gold-standard TDI map (TDI_{GS}) with 0.8 mm isotropic resolution (and calculated from 0.8 mm source diffusion MRI data); (third column) low-resolution TDI map (TDI_{LR}) with 2.4 mm isotropic resolution (and calculated from 2.4 mm source diffusion MRI data); (fourth column) super-resolution TDI map ($superTDI_{LR}$) with 0.8 mm isotropic resolution (and calculated from 2.4 mm source diffusion MRI data). The bottom row show the corresponding directionally-encoded color (DEC) TDI maps (red: left-right, green: anterior-posterior, blue: inferior-superior). As shown in the figure, several brain structures are recovered by the super-resolution step; furthermore, these structures could not have been defined based on the anatomical information contained in the low-resolution TDI_{LR} map. SLF: superior longitudinal fasciculus.

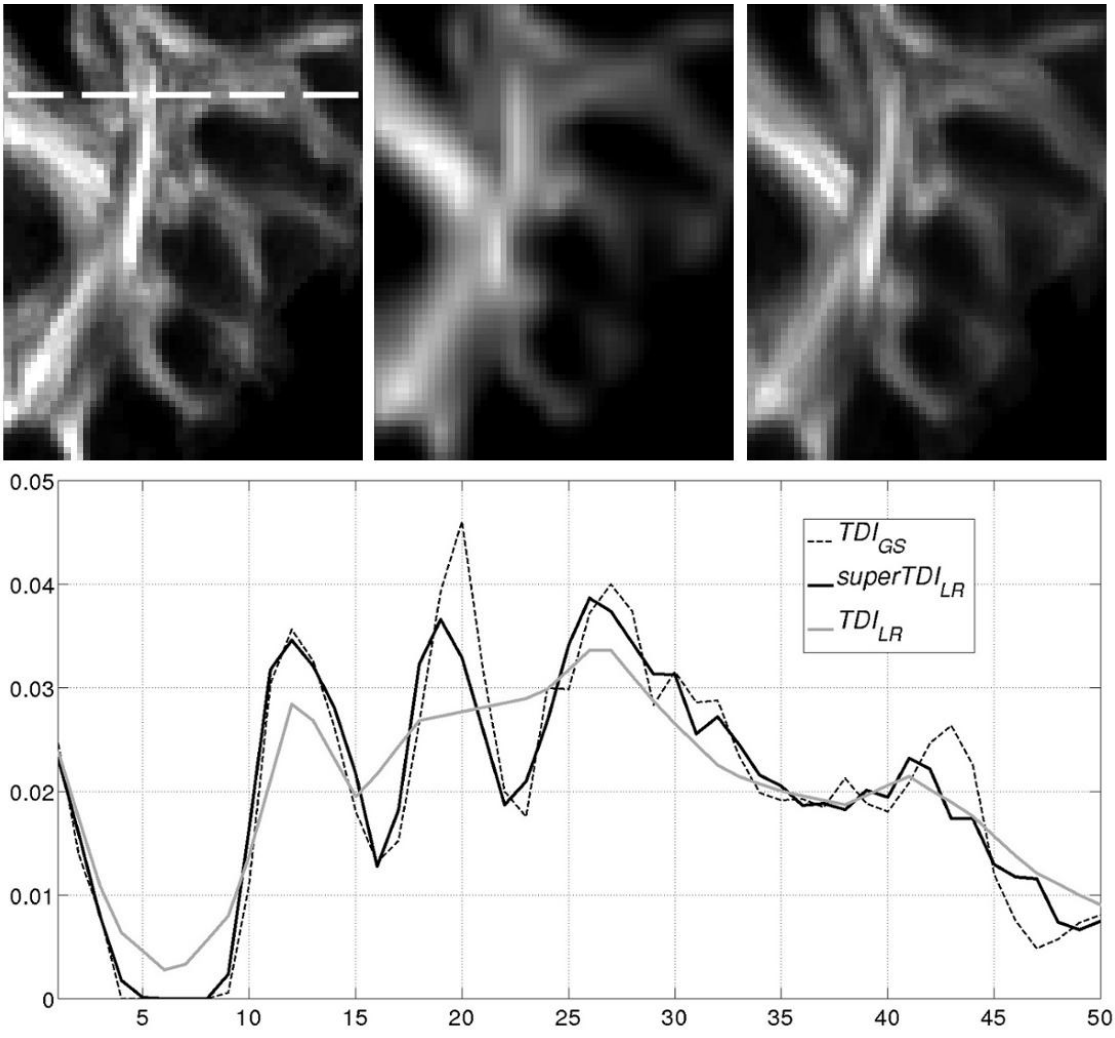

Fig. 4: TDI profiles through a horizontal level (see dashed line) of the same parietal-occipital white matter region as shown in Fig. 3. Top row: (left) gold-standard TDI map (TDI_{GS}) with 0.8 mm isotropic resolution (and calculated from 0.8 mm source diffusion MRI data); (middle) low-resolution TDI map (TDI_{LR}) (with 2.4 mm isotropic resolution and calculated from 2.4 mm source diffusion MRI data) interpolated to 0.8 mm resolution; (right) super-resolution TDI map ($superTDI_{LR}$) with 0.8 mm isotropic resolution (and calculated from 2.4 mm source diffusion MRI data). The bottom graph shows the corresponding profiles at the

level shown by the dashed line (see top left image). The profile from the super-resolution data (black solid line) recovers the main features of the gold-standard case (black dashed line); this is not the case for the interpolated low resolution data (gray solid line). For visualisation purpose, the 3 profiles where normalised to have the same area under the curve.

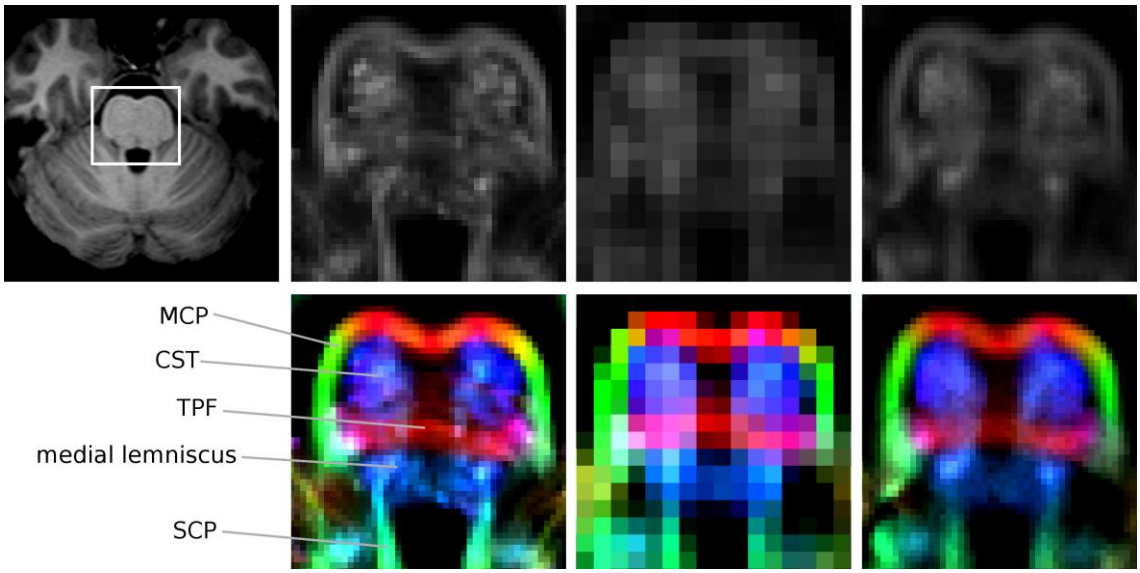

Fig. 5: Structures identified by the super-resolution step at the level of the pons. Top row: (first column) anatomical T1-weighted image indicating the zoomed region shown in the TDI maps; (second column) gold standard TDI map (TDI_{GS}) with 0.8 mm isotropic resolution (and calculated from 0.8 mm source diffusion MRI data); (third column) low-resolution TDI map (TDI_{LR}) with 2.4 mm isotropic resolution (and calculated from 2.4 mm source diffusion MRI data); (fourth column) super-resolution TDI map ($superTDI_{LR}$) with 0.8 mm isotropic resolution (and calculated from 2.4 mm source diffusion MRI data). The bottom row show the corresponding directionally-encoded color (DEC) TDI maps (red: left-right, green: anterior-posterior, blue: inferior-superior). As shown in the figure, several brain structures are recovered by the super-resolution step. MCP: middle cerebellar peduncle, CST: corticospinal tract, TPF: transverse pontine fibres, SCP: superior cerebellar peduncle.

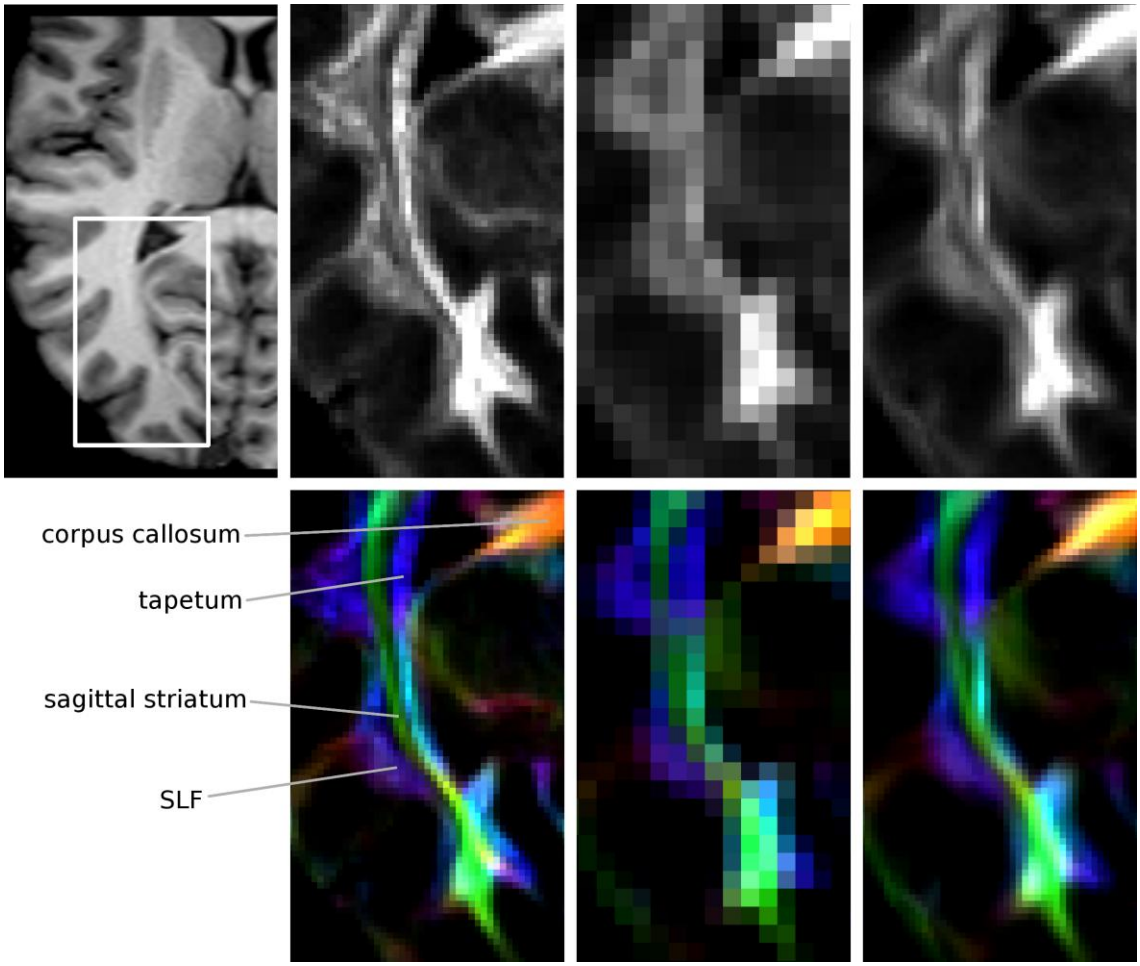

Fig. 6: Structures identified by the super-resolution step at the level of the optic radiation. Top row: (first column) anatomical T1-weighted image indicating the zoomed region shown in the TDI maps; 19 (second column) gold standard TDI map (TDI_{GS}) with 0.8 mm isotropic resolution (and calculated from 0.8 mm source diffusion MRI data); (third column) low-resolution TDI map (TDI_{LR}) with 2.4 mm isotropic resolution (and calculated from 2.4 mm source diffusion MRI data); (fourth column) super-resolution TDI map ($superTDI_{LR}$) with 0.8 mm isotropic resolution (and calculated from 2.4 mm source diffusion MRI data). The bottom row show the corresponding directionally-encoded color (DEC) TDI maps (red: left-right, green: anterior-posterior, blue: inferior-superior). As shown in the figure, several brain structures are recovered by the super-resolution step. SLF: superior longitudinal fasciculus.

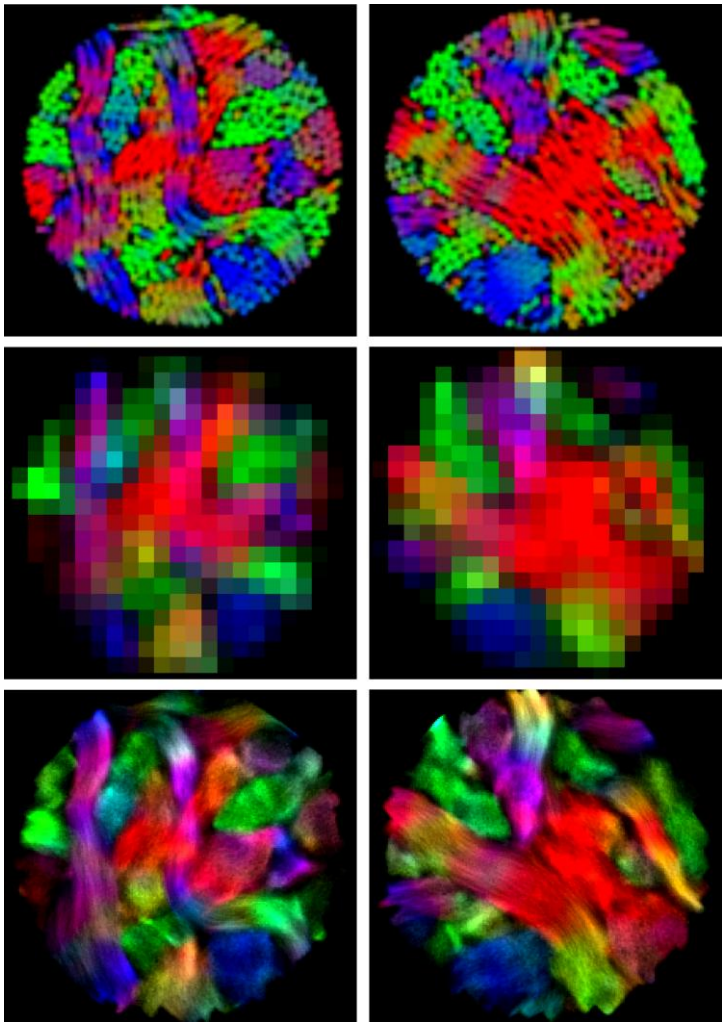

Fig. 7: Directionally-encoded color (DEC) TDI maps for two tilted-slices through the numerical phantom (each column of the figure corresponds to a slice). Top-row: simulated structures. (Middle-row) DEC TDI map created without super-resolution (2 mm isotropic grid). (Bottom-row) DEC TDI map created with super-resolution (0.2 mm grid). Many of the features of this complex structure (shown in the top-row) are recovered by the super-resolution step (bottom-row), and cannot be discerned in the map created without super-resolution (middle-row). The color-coding indicates the main local orientation, defined based on the streamlines contained in the grid element for the TDI cases shown in the middle and bottom rows.

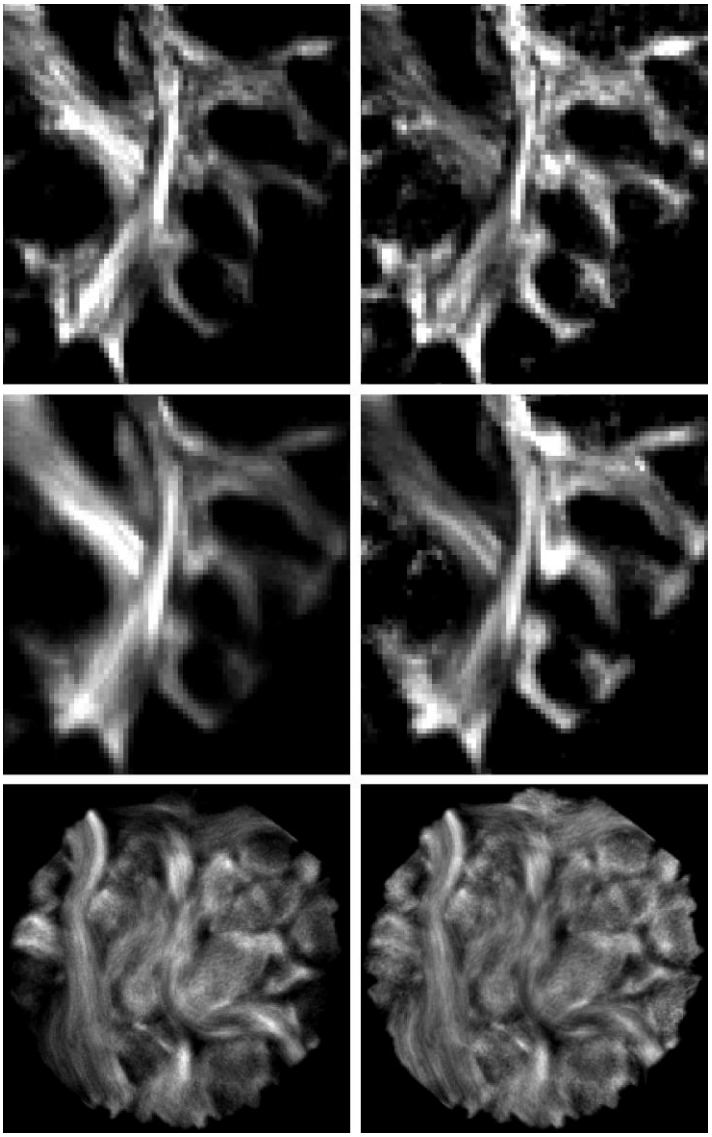

Fig. 8: Comparison of standard TDI maps (left column) and length-scaled TDI maps (*ls*TDI) (right column). The top and middle rows show *in vivo* examples in the parietal-occipital white matter (same area as that shown in Fig. 3): the top row corresponds to the gold-standard maps with 0.8 mm isotropic resolution (and calculated from 0.8 mm source diffusion MRI data); the middle row corresponds to the super-resolution maps with 0.8 mm isotropic resolution (and calculated from 2.4 mm source MRI data). The bottom row shows the super-resolution (0.2 mm grid) results for an *in silico* example (same slice as that shown in the left column of Fig. 6). The *ls*TDI maps show relatively increased intensity for shorter tracks and relatively decreased intensity for longer ones compared to the same regions in the TDI maps.

DISCUSSION

This study validates the super-resolution property of the TDI method (i.e. it answers *question (1)* in the Introduction). Using *in vivo* 7 Tesla diffusion data, the brain structures that could be identified in the TDI_{LR} map *only* after using super-resolution (i.e. in the *super-*TDI_{LR} map) were consistent with the corresponding structures identified in the gold-standard TDI map (i.e. in the TDI_{GS} map). This supports the claim that structures generated by the super-resolution step are not an artefact of the super-resolution process itself. These findings were also consistent with those found in the *in silico* data, where structural features delineated in the super-resolution TDI map of the numerical phantom were consistent with those simulated. In fact, the phantom data provides a striking example of the structural improvement retrieved by super-resolution TDI: most of the fiber bundles are not even identifiable in the low-resolution data (Fig. 7, middle-row), but they are clearly distinguished in the super-resolution data (bottom-row). It should be noted that conventional interpolation methods do not add such extra information, but have a mainly 'cosmetic', edge smoothing effect, as discussed in (Calamante et al., 2010).

It should be noted, however, that the *in vivo* 0.8 mm *super-*TDI_{LR} maps are not exactly the same as the 0.8 mm TDI_{GS} maps (see Figs. 3-6). The super-resolution approach cannot fully recover the information contained in the *acquired* higher resolution data: there is some loss of fine detail, and the *super-*TDI_{LR} map is a slightly blurred version of the TDI_{GS} map. This is not surprising, considering the larger tractography errors expected when performing fibre-tracking on lower-resolution diffusion MRI data. For example, there could be differences in the fibre-orientations identified by CSD, due to the increased partial volume effects at lower resolution. As might be expected, the level of blurring is dependent on the amount of down-sampling; for example, down-sampling the data by a factor of 2 (from 0.8 mm to 1.6 mm) led to less blurring and the super-resolution results were closer to the gold-standard (data not shown). Nevertheless, given the practical impossibility of acquiring high-resolution diffusion MRI data for most applications, the super-resolution TDI method provides a very powerful practical alternative. Furthermore, validation of the super-resolution property provides support to the veracity of the structures that are visualised at even smaller reconstructed voxel size (e.g. at the 125 μm isotropic resolution included in the original study (Calamante et al., 2010)), which cannot be achieved whole-brain by acquisition methods in practical situations. Therefore, the findings from this study provide further support for the potential use of the TDI technique to study the brain and its disorders.

It should also be noted that the super-resolution TDI method is able to achieve super-resolution in white matter only when applied to structures with different orientations. For example, if there is a very narrow gap between similarly-oriented structures (as is the case between the smaller strands that together constitute the fasciculus-like larger bundles in the numerical phantom, e.g. see top-row of Fig. 7), super-resolution TDI will not be able to resolve it. Probabilistic fibre-tracks can interchange between adjacent similarly-oriented fibres. Since TDI is based on the fibre-tracking model, super-resolution TDI relies on white matter bundles with different orientations to achieve super-resolution at their interface.

The *in vivo* validation part of this study was feasible due to the use of ultra-high field MRI technology (i.e. 7 Tesla MRI). While the total acquisition time (69 min) and the relatively low SNR were not ideal, acquisition of an equivalent data-set at 3 Tesla would have been completely impractical. Similarly, the use of more common lower-resolution diffusion MRI data at 3 Tesla (e.g. 2.4 mm isotropic) would have not been suitable for the down-sampling analysis methodology used in our study: a 3-fold down-sampled voxel size (~7 mm) would have been too coarse to characterise the distribution of fibre orientations (e.g. fibre-curving

within the voxel would have been much more significant), thus introducing larger errors in fibre-tracking. However, it should be noted that the acquired 7 Tesla data are not optimal for TDI, as can be appreciated from the higher quality of the TDI maps previously produced at 3 Tesla with a much shorter acquisition protocol (Calamante et al., 2010). Given the increased susceptibility-related distortions, shorter T2, and longer T1 at 7 Tesla, and the fact that the diffusion contrast mechanism is B_0-independent, 3 Tesla currently may be a more suitable magnetic field strength for TDI. Future developments in 7 Tesla may compensate for some of these limitations.

It should be noted that short fibre-bundles tend to have fewer tracks due to the random seed-point placement strategy; the latter leads to reduced intensity in the standard TDI map due to the lower number of seeds (and thus tracks) generated in these bundles (see Fig. 8). While this effect is most easily appreciated in the phantom data (see peripheral short bundles with low intensity in Fig. 7), it is also present for short bundles in the *in vivo* data (e.g. Fig. 8). The *ls*TDI method introduced in this work provides a simple way to mitigate this effect (i.e. by weighting the contribution from each track to the TDI value by the inverse of its length). As expected, the TDI contrast is modified by this normalisation (see Fig. 8), although both TDI approaches still maintain high contrast. Furthermore, the lower contribution to the intensity from the *ls*TDI method leads to an overall slightly lower SNR; this can be compensated by increasing the total number of tracks generated during the fibre-tracking step, as shown for the standard TDI method (Calamante et al., 2010). We speculate that the original TDI technique is likely to be more appropriate for studies where the anatomical detail is of interest (due to the increased contrast in long bundles), while the *ls*TDI method is possibly more appropriate for studies where quantification is sought (e.g. voxel-based analysis) due to the reduce sensitivity of the map intensity to the track-length. However, it remains to be shown which of the two TDI approaches will prove more useful in practice, and it is likely that this will be dependent on the particular application of interest.

The comparison presented in this work was performed qualitatively. A quantitative comparison of TDI maps from different protocols (e.g. different base spatial resolution, such as the LR and HR data-sets in the current study) is not straightforward due to the influence of experimental conditions on FOD estimation, probabilistic tracking results, and TDI values. It is well-known that the acquisition parameters and image quality affect the accuracy and precision with which fibreorientations are estimated in a voxel (Tournier et al., 2007). For example, in our case, both the different spatial resolution and SNR will have an effect on the FOD calculated using CSD. The FODs will, in turn, have a direct influence in the quality of the fibre-tracking (e.g. wider FODs will lead to more spread fibre-tracking results using probabilistic fibre-tracking). Since the TDI map is calculated from the fibre-tracking results, the actual TDI values cannot be compared between data acquired with different acquisition parameters (or similarly, with different post-processing parameters). It should be emphasised a principal role for the TDI technique is as an imaging modality that can be used for improved delineation of brain features (due to its high-resolution and anatomical contrast), for which a qualitative comparison is appropriate. On the other hand, as discussed in our earlier work (Calamante et al., 2010), there may also be a *quantitative* role for the super-resolution TDI technique, provided future studies show the method to have good quantitative reproducibility. In fact, recent work (Bozzali et al., 2011) has used an approach that has similarities to the TDI method (albeit without involving super-resolution), and demonstrated its potential role in voxel-based analysis.

The basic idea of counting tracks has been around in diffusion MRI for several years (e.g., (Behrens et al., 2003; Roberts et al., 2005; Thomas et al., 2005)). These earlier studies used track-density quantification to estimate the probability of connection between regions, as a

tool to parcellate brain structures from probabilistic tractography results, or as a summary parameter to characterise fibre bundles for intra- and inter-subject quantitative analysis. In the super-resolution TDI methods, track-density mapping is not used for a particular white matter structure, but is used to calculate high-quality whole-brain track-density maps, with higher anatomical and spatial information than the source diffusion images used to generate the maps (i.e. the track-density is used as a means to achieve super-resolution). Therefore, it is a fundamentally different use of the information that can be derived from the track-counting.

The super-resolution TDI technique not only can play a role in the direct visualization of brain sub-structures, but could also have important applications as a complementary tool for fibre-tracking studies (e.g. by aiding placement of seed/target regions due to the fine anatomical detail and high-spatial resolution), inter-subject spatial normalisation, assessment of changes in brain connectivity (as defined by whole-brain fibre-tracking results), and voxel-based analyses. A more detailed description of the potential applications of the TDI technique can be found in Calamante et al., 2010.

While the current study validates the super-resolution properties of the TDI technique, validation of the anatomical information-content in the TDI contrast (see *question 2* in the Introduction) would ideally involve a comparison with an *anatomical* 'gold-standard'. Further studies are therefore needed to address this aim; for example, imaging excised brains and comparing the results to histological brain sections would provide a rigorous validation to the anatomical informationcontent of the TDI contrast.

In summary, we have validated the *super-resolution property* of the TDI method, thus providing further evidence for the potentially important role of this methodology in neuroscience. Furthermore, an alternative version of the TDI technique (*ls*TDI) was introduced, which mitigates the dependence of the TDI map intensity on the track-length, and may therefore be more suited for quantitative studies.

A C K N O W L E D G E M E N T S

FC, J-DT, GDJ, and AC are grateful to the National Health and Medical Research Council (NHMRC) of Australia, Austin Health, the Brain Research Institute Foundation, and the Victorian Government's Operational Infrastructure Support Program for their support. RMH thanks Josef Pfeuffer and Thorsten Feiweier from Siemens Healthcare for technical support. Part of the work performed at the 7 Tesla is supported by the FET project CONNECT of the European Union.

R E F E R E N C E S

Behrens, T.E., Johansen-Berg, H., Woolrich, M.W., Smith, S.M., Wheeler-Kingshott, C.A., Boulby, P.A., Barker, G.J., Sillery, E.L., Sheehan, K., Ciccarelli, O., Thompson, A.J., Brady, J.M., Matthews, P.M., (2003). Non-invasive mapping of connections between human thalamus and cortex using diffusion imaging. *Nature Neurosci.* **6**, 750–757.

Bozzali, M., Parker, G.J., Serra, L., Embleton, K., Gili, T., Perri, R., Caltagirone, C., Cercignani, M., (2011). Anatomical connectivity mapping: A new tool to assess brain disconnection in Alzheimer's disease. *NeuroImage*. 2011;54(3):2045-2051

Calamante, F., Tournier, J.-D., Jackson, G.D., Connelly, A., (2010). Track Density Imaging (TDI): Super-resolution white matter imaging using whole-brain track-density mapping. *NeuroImage* **53**, 1233-1243.

Close, T.G., Tournier, J.-D., Calamante, F., Johnston, L.A., Mareels, I., Connelly, A., (2009). A software tool to generate simulated white matter structures for the assessment of fibre-tracking algorithms. *NeuroImage* **47**, 1288–1300.

Greenspan, H., Oz, G., Kiryati, N., Peled, S., (2002). MRI inter-slice reconstruction using super resolution. *Magn Reson Imaging* **20**, 437–446.

Gudbjartsson, H., Patz, S., (1995). The Rician Distribution of Noisy MRI Data. *Magn Reson Med.* **34**, 910–914.

Heidemann, R.M., Anwander, A., Knoesche, T., Feiweier, T., Fasano, F., Pfeuffer, J., Turner, R., (2010). Isotropic High Resolution Diffusion-Tensor Imaging in Humans at 7T. *In: Proc. 18th Annual Meeting of the Int. Soc. Magn. Reson. Med. (ISMRM)*, Stockholm, Sweden, 2010; **18**, p. 1610.

Henkelman, R.M., (1985). Measurement of signal intensities in the presence of noise in MR images. *Med Phys.* **12**, 232–233. [Erratum in **13**, 544 (1986)].

Hwang, T.-L., van Zijl, P.C.M., Garwood, M., (1999). Asymmetric Adiabatic Pulses for NH Selection. *J. Magn. Reson.* **138**, 173-177.

Jenkinson, M., Bannister, P., Brady, M., Smith, S. (2002). Improved optimization for the robust and accurate linear registration and motion correction of brain images *NeuroImage* **17**, 825–841.

Pajevic, S., Pierpaoli, C., (1999). Color schemes to represent the orientation of anisotropic tissues from diffusion tensor data: application to white matter fiber tract mapping in the human brain. *Magn Reson Med.* **42**, 526-540.

Peled, S. Yeshurun, Y., (2001). Superresolution in MRI: Application to Human White Matter Fiber Tract Visualization by Diffusion Tensor Imaging. *Magn. Reson. Med.* **45**, 29–35.

Peled, S. Yeshurun, Y., (2002). Superresolution in MRI—Perhaps Sometimes. *Magn. Reson. Med.* **48**, 409–409.

Pfeuffer, J., van de Moortelle, P., Yacoub, E., Adriany, G., Andersen, P., Merkle, H., Garwood, M., Ugurbil, K., Hu, X., (2002). Zoomed functional imaging in the human brain at 7 Tesla with simultaneously high spatial and temporal resolution. *NeuroImage* **17**, 272-286.

Roberts, T.P., Liu, F., Kassner, A., Mori, S., Guha, A., (2005). Fiber density index correlates with reduced fractional anisotropy in white matter of patients with glioblastoma. *AJNR Am J Neuroradiol.* **26**, 2183-2186.

Scheffler, K., (2002). Superresolution in MRI? *Magn. Reson. Med.* **48**, 408–408.

Stejskal, E.O., Tanner, J.E., (1965). Spin diffusion measurements: spin echoes in the presence of a time-dependent field gradient. *J. Chem. Phys.* **42**, 288-292.

Talairach, J., Tournoux, P., (1988). Co-Planar Stereotaxic Atlas of the Human Brain: 3-Dimensional Proportional System: An Approach to Cerebral Imaging. Thieme Medical Publishers.

Thomas, B., Eyssen, M., Peeters, R., Molenaers, G., Van Hecke, P., De Cock, P., Sunaert, S., (2005). Quantitative diffusion tensor imaging in cerebral palsy due to periventricular white matter injury. *Brain.* **128**, 2562-2577.

Tournier, J.D., Calamante, F., Connelly, A., (2007). Robust determination of the fibre orientation distribution in diffusion MRI: non-negativity constrained super-resolved spherical deconvolution. *NeuroImage.* **35**, 1459-1472.

Tournier, J.D., Calamante, F., Connelly, A., (2010). Improved probabilistic streamlines tractography by 2nd order integration over fibre orientation distributions. *In: Proc. 18th Annual Meeting of the Intl. Soc. Mag. Reson. Med. (ISMRM)*, Stockholm, Sweden, 2010; **18**, p.1670.

Tournier, J.D., Calamante, F., Gadian, D.G., Connelly, A., (2004). Direct estimation of the fibre orientation density function from diffusion-weighted MRI data using spherical deconvolution. *NeuroImage*. **23**, 1176–1185.

Tournier, J.D., Yeh, C.H., Calamante, F., Cho, K.H., Connelly, A., Lin, C.P., (2008). Resolving crossing fibres using constrained spherical deconvolution: Validation using diffusion-weighted imaging phantom data. *NeuroImage* **42**: 617–625.